AIAA JOURNAL
Vol. 31, No. 3, March 1993

Application of Particle Image Velocimetry in High-Speed Separated Flows

M. J. Molezzi* and J. C. Dutton†
University of Illinois at Urbana-Champaign, Urbana, Illinois 61801

A particle image velocimetry (PIV) system has been developed for use in high-speed separated air flows. The complete system was developed to improve the spatial resolution and accuracy of the PIV technique as applied in high-speed compressible flows and is the first to incorporate both birefringent image shifting and submicron seed particles for analysis of separated flowfields. The system has been proven in preliminary experiments using a simple low-speed round jet flow and has been validated for accuracy with both known displacement simulated PIV photographs and with uniform flow experiments at Mach 0.5 (170 m/s) for comparison with pressure and laser Doppler velocimeter data. PIV data have also been obtained in the separated wake region behind a two-dimensional base model in a Mach 0.4 freestream flow (135–220 m/s) with resolution of velocity in 1.0-mm^2 regions, revealing features of the von Kármán vortex street wake and underlying small-scale turbulence.

Introduction

EXPERIMENTAL investigation of turbulent and compressible flows has become increasingly sophisticated in recent years with the advent of laser based measurement techniques. Among these tools is a relatively new technique called particle image velocimetry (PIV). PIV is performed by illuminating a seeded flowfield with a planar laser sheet that is pulsed at a known time interval, forming two or more images of each seed particle within the light sheet (Fig. 1). After recording these images on film or another medium, image separations and therefore velocities can be determined for the entire plane. Unlike pointwise techniques such as laser Doppler velocimetry (LDV) which provides statistical velocity data on a point-by-point basis, PIV can identify instantaneous flow structures that may be random in nature but important to the overall behavior of the flow. PIV also reveals planar views of three-dimensional flow structures that are smeared by volume integration inherent in techniques such as schlieren photography. Other advantages include the ability to obtain PIV images quickly, allowing shorter run times, larger test sections, and higher Mach numbers.

Although molecular imaging techniques have recently been used for high-speed velocity measurements,[1,2] pioneering work by Kompenhans and Höcker[3,4] and Post et al.[5] have recently extended the particle-based PIV technique to high-speed flows. Despite this initial work, difficulties in seeding and image acquisition have limited the spatial resolution of PIV. One of the most important considerations in PIV for high-speed flow applications is obtaining adequate seed density for successful interrogation at all locations. Since most high-speed wind tunnels are not recirculatory, high seed density can only be obtained by injecting a large mass of seed with the flow. Local seeding in areas of interest can be a solution, but injection may need to be done upstream of flow conditioning devices and nozzles that partially disperse the seed. Difficulty also arises in obtaining sufficient seeding in separated zones of the flow (behind bases, steps, etc.). Experience with both PIV and LDV shows that seed density in these areas is generally sparse, causing significant data dropout. Another concern is the choice of seed particles that are small enough to follow large velocity gradients while still scattering sufficient light to expose film. The seeding material is further restricted when birefringent image shifting[6] is used to resolve the directional ambiguity of image displacements in high-speed separated flows. Image shifting involves shifting the second image of every particle by a known distance to assure that the direction of image displacement is known over the entire PIV photograph. Birefringent image shifting is done by using vertically and horizontally polarized light for the two illumination pulses, then photographing the flowfield through a birefringent calcite crystal that shifts one polarization of light (and therefore one set of images) by a known distance. This use of polarized light sources requires seed particles which maintain polarization in sidescatter. After image displacements are determined from the photograph, the "shift displacement" is subtracted off to return the actual flowfield displacements (and velocities).

Laser requirements are also a factor in the use of PIV for high-speed flow applications. To illuminate small seed particles, high power in the visible spectrum is a necessity. Kompenhans and Höcker[3,4] have used a Nd:YAG system with 70 mJ/pulse for recording images on 35-mm film, but when necessary, resolution of small-scale velocity fluctuations in high-speed test sections requires the use of large format film to reduce diffraction-limited image sizes and to avoid film grain limitations. The larger film area, in turn, requires much greater illumination. The high laser energy must also be combined with very short pulse duration to prevent image blur which reduces the accuracy of velocity measurements. Typical super-

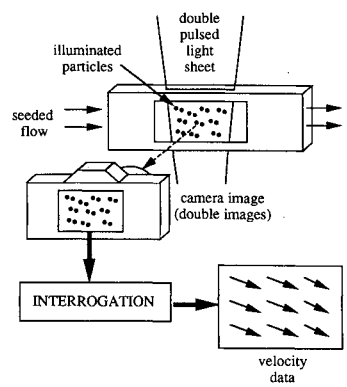

Fig. 1 Principle of PIV.

Presented as Paper 92-0004 at the AIAA 30th Aerospace Sciences Meeting, Reno, NV, Jan. 6–9, 1992; received March 17, 1992; revision received May 26, 1992; accepted for publication June 12, 1992.

*Graduate Research Assistant, Department of Mechanical and Industrial Engineering. Student Member AIAA.

†Professor, Department of Mechanical and Industrial Engineering. Associate Fellow AIAA.

sonic flow speeds require laser pulse durations on the order of 10 ns or less.

With consideration of the aforementioned factors for PIV application, the present work sets out to advance the capabilities of the PIV technique as applied in high-speed flows. Specifically, the objectives include improvement of the spatial resolution of velocity measurements on a uniform grid to improve detection of small-scale instantaneous structures. The technique is also applied in fully separated flowfields where recirculatory, unsteady, instantaneous structures can dominate the fluid dynamic behavior. These applications involve careful choice of the seeding material and delivery system and the implementation of birefringent image shifting. Finally, the importance of obtaining highly accurate data for quantitative analysis requires careful system validation and determination of data accuracy.

Particle Image Velocimetry Equipment and Operation

Acquisition System

The acquisition system refers to the equipment used to obtain double-exposed particle image photographs of the flowfield of interest. Diagrams of the PIV acquisition system equipment and beam optics are shown in Fig. 2. This system uses two Continuum YG681C-10 Nd:YAG lasers equipped with frequency doubling crystals to provide a maximum output energy of 550 mJ/pulse at a wavelength of 532 nm (green light) with a pulsewidth of 4–6 ns. High-resolution black-and-white films are very sensitive to green wavelengths and the high visibility of the green light also simplifies alignment of the two beams, which is a critical factor in obtaining double exposures of particles in the flow. Two separate lasers are required since a single laser cannot generate two distinct, equal energy pulses in the short time interval required for high-speed flows (typically less than 1 μs). The horizontally and vertically polarized beams of the two lasers are combined by a polarized beam splitter, then shaped by spherical and cylindrical lenses to form a planar beam profile with a waist thickness of 0.4 mm. Beam thickness can be increased by positioning the beam waist either above or below the test section. Beam width at the test section is adjustable up to 125 mm by positioning the 300-mm cylindrical lens. All lenses are made from fused silica substrate and all optics use high-power Nd:YAG coatings to limit beam energy loss to less than 0.25% per surface.

The photographic recording of particle images is done by a camera mounted on the same optical table as the lasers and beam shaping optics. This allows maintenance of the relative position of all optical components for consistent alignment

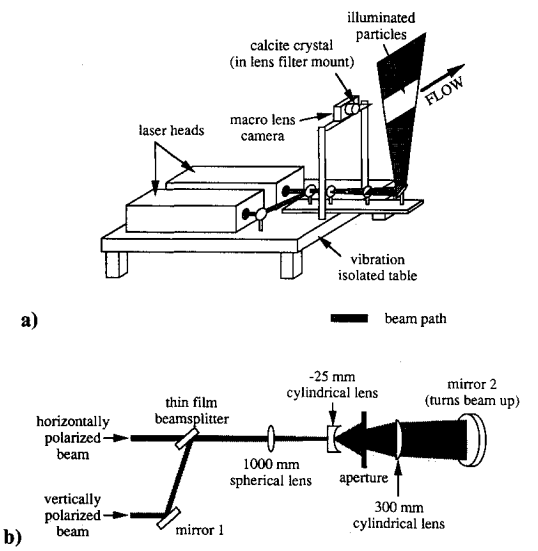

Fig. 2 PIV acquisition system: a) laser and camera equipment for acquiring PIV photographs; b) top view of laser optics for forming planar beam profile.

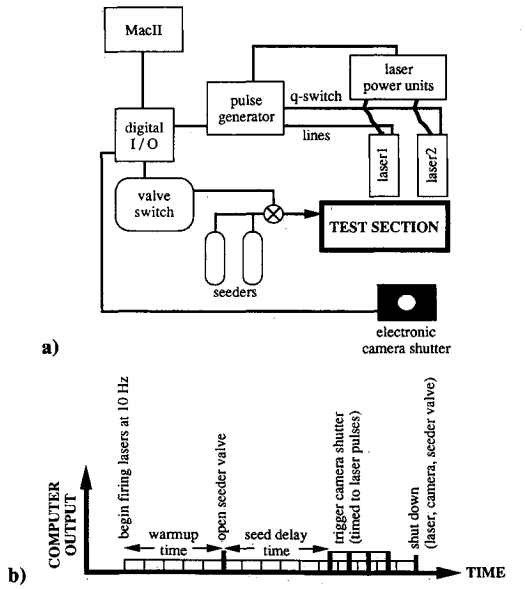

Fig. 3 Acquisition system control: a) equipment schematic; b) timing diagram for automated acquisition of PIV photographs.

and focus. This table is also mounted on vibration-isolated supports to avoid the effects of laboratory vibrations. The system can use a 35 mm, 6×8 cm, or 4×5 in. camera. The 35 mm and 6×8 cm cameras have 100- and 300-mm macro lenses, respectively, and both have auto film wind and an electronic shutter for automated operation. The system has also been used with a modified 4×5 in. camera with a manual shutter and 120-mm macro lens, but since it can take only one frame before reloading, its large format film is most useful when the highest possible resolution of particle images for determination of small-scale turbulent motions is necessary. Flat-field or macro lenses are required to prevent distortion of the field of view at the edges which would induce error in the measurement of particle displacements. Long focal length lenses are used to reduce the solid angle from the lens to the field of view, thereby minimizing parallax. For given flowfield dimensions, longer focal length lenses are required for larger format films to maintain a constant solid angle. In the case of the 4×5 in. camera, a longer focal lens would be desirable, but since none was available the experiments done with this camera used a laser sheet with half the thickness used for other experiments, thereby effectively reducing parallax.

Automation of the system is a key for allowing acquisition of multiple photographs in short run-time test sections, thereby randomly capturing unsteady structures in various stages of development. Control of this system is done by a Macintosh II computer equipped with a digital input/output board and solid state module switches (Fig. 3a). Computer software controls the triggering of the lasers via a Stanford Research pulse generator, an electro-pneumatic valve to release seed into the test section, and the camera shutter. The timing diagram in Fig. 3b indicates the sequence of events controlled by the computer system. Software allows the user to select the warmup time (for laser warmup and wind tunnel adjustment), the seed delay time (to allow seed to propagate from the seeder valve to the test section), and the number of photographs desired. Since the pulse rate of the lasers must be fixed at 10 Hz, conditional sampling of PIV by external events would only be possible for periodic events, in which case software could be implemented to predict from input data when an event would coincide with a laser pulse, factoring in delay times from all inputs and outputs.

Interrogation System

After PIV negatives are obtained and processed for high contrast (to increase signal-to-noise ratio) and contact printed

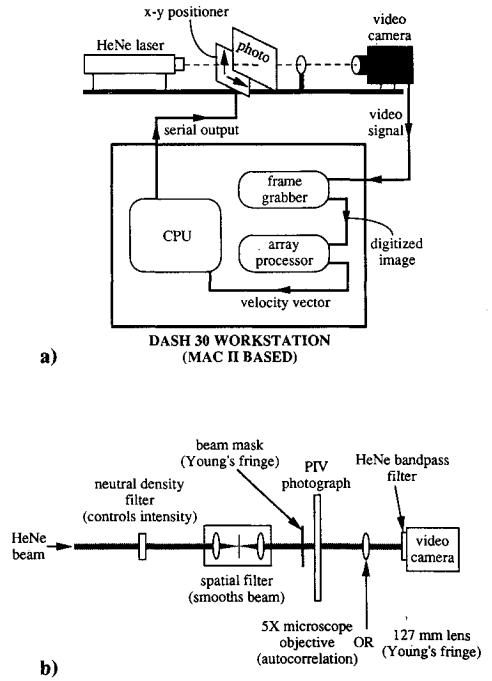

Fig. 4 PIV interrogation system: a) equipment schematic; b) optical components.

onto film to obtain positive images, the photographs are examined using an automated interrogation system controlled by a "Dash 30" modified Macintosh II computer operating at 50 MHz. Diagrams of the interrogation system and the accompanying optics are shown in Figs. 4a and 4b.

Simply explained, the average particle displacement for an interrogation spot is determined from its spatial autocorrelation function, which is derived by performing two two-dimensional Fourier transforms.[7] This is most commonly done by either the "Young's fringe" method where the first transform is done optically and the second is done digitally by fast Fourier transform (FFT), or the "autocorrelation" method where the original interrogation spot is digitized and both transforms are done by digital FFTs. Although the Young's fringe method is faster, the autocorrelation method provides the advantages of easier setup and increased flexibility. Imaging the interrogation spot to the video camera allows control over image focus, image contrast, and interrogation spot size by direct observation. Use of the Young's fringe method requires collimation of the illuminating beam to obtain good interference fringes from the optical transform, beam masking to select the spot size, and the relatively difficult task of determining the "best" fringe pattern by adjustment of optics, beam focus, and beam intensity. The speckle in typical fringe patterns (caused by coherent light interference) makes this task difficult, and if not done well, it can significantly reduce the number of successful interrogations on a given PIV photograph. An additional advantage of the autocorrelation method is that both the original particle images and the autocorrelation output can be digitally recorded for a particular interrogation spot, allowing the user to physically measure the particle displacements and compare to the system output for accuracy. For these reasons and the fact that interrogation time constraints are not particularly important in comparison to other processing tasks, the autocorrelation method is used for the data presented in this paper.

For this system, the completed PIV photograph is mounted between glass plates on a two-dimensional Aerotech positioner system to scan the photograph spot by spot with a fixed 5-mW HeNe illumination beam and optics. The HeNe beam is passed through a neutral density filter to control intensity, then it is spatially filtered to eliminate high-frequency intensity variations that could add noise to the illuminated interrogation spot. If the Young's fringe method is being used, the beam then passes through a mask to determine the interrogation spot size. After passing through the photograph, an imaging lens is then chosen to obtain either the actual particle images or the far-field diffraction pattern (optical Fourier transform) of the interrogation spot, depending on the interrogation method being used. A 5X microscope objective lens is used to obtain particle images, while a 127-mm plano-convex lens is used to obtain the optical Fourier transform. Finally, the image is received by a Sierra Scientific CCD array video camera with a HeNe bandpass filter to eliminate room light interference. The choice of a HeNe laser is made to ensure uniform illumination by use of the spatial filter, to allow interrogations in normal room light conditions by using the HeNe bandpass filter, and to provide the collimated light source required when Young's fringe interrogations are desired.

The video image is then digitized to a 512×512 pixel array by a Perceptics frame grabber board with 8-bit grayscale (256 gray levels) and is passed to a Mercury MC3200-NU array processor which performs FFTs and other array operations to obtain the two-dimensional autocorrelation of the original image. The array processor uses a centroidal peak-finding routine to locate up to three of the strongest autocorrelation peaks. These peak locations are stored as the most likely image displacements for that interrogation spot and the process is repeated for the next spot.

After the full vector field is determined, postprocessing must be done to refine the data. As a first pass, the vector field is checked by a routine that looks for "bad" vectors that are outside user-specified absolute limits and replaces them with one of the secondary peaks for that location if it is acceptable, or with a default value to indicate a bad measurement. The few remaining spurious velocity vectors are manually removed and replaced with the aforementioned default value. Another automated routine then searches for default values and replaces them with values interpolated from valid neighboring vectors using multiple linear regression. The vector field is then smoothed by convolution with a Gaussian kernel as described by Landreth and Adrian[8] to eliminate random noise in the vector field caused by image imperfections, video noise, and other factors. This is crucial when spatial differentiation is to be performed on the vector field to derive quantities such as vorticity, since any high-frequency random error will be accentuated by differentiation.

Flow Seeding

The choice of a seeding material and delivery system is key to the successful implementation of PIV in high-speed flows. The limitations of particle techniques hinge on production of particles with sufficiently low slip velocity to accurately follow high-velocity gradients in compressible flows. This also affects the ability of seed to be carried into separated flow regions where vortices tend to throw heavy particles out, thereby reducing seed density. The density of seed in areas of interest also places a limitation on the spatial resolution of velocity measurements. An additional factor is the ability of the particles to scatter sufficient light for PIV photographs, which is dependent on particle shape and refractive index. In the development of this system, various seed materials have been examined for slip velocity and optical performance, including atomized water, atomized silicone oil, and monodispersed polystyrene latex (PSL) spheres of various sizes. Each seed type was used for test photographs and all were successfully recorded on film including 0.5- and 1.0-μm-diam monodispersed PSL spheres. The resulting choice for high-speed flow experiments was silicone oil seed generated by a six-jet atomizer made by TSI, Inc. The polydispersed atomized droplets have a mean diameter of 0.8 μm as quoted by TSI and Bloomberg,[9] and show good response to the velocity gradient across an oblique shock wave.[9] PSL spheres of 0.5 and 1.0 μm diameter also respond well to velocity gradients, but cannot be delivered in large enough quantities for PIV requirements.

Test photographs also show good performance of the silicone oil droplets for image exposure intensity and for birefringent image shifting. The seed delivery system used for the transonic wind-tunnel experiments presented here is a localized multiple-tube arrangement described in further detail in the discussion of experimental results.

Spatial Resolution

In a high image density PIV system, each individual velocity vector is determined by the mean particle displacement in the interrogation spot. Therefore, the spatial resolution of a data-set is determined by the interrogation spot size as measured in the flowfield frame of reference. To use a particular spot size, for example 1×1 mm, many requirements must be satisfied. First, the diameter of the particle images must be small enough to measure displacements greater than one image diameter within the spot, since overlapping images cannot be distinguished. Second, the maximum displacement should be less than approximately 25% of the linear dimension of the spot,[7] in this case 250 μm, to insure that a sufficient number of image pairs will appear fully within the spot for successful interrogation. This is accomplished by selecting the proper time delay between laser pulses for a given flowfield photograph. Finally, the particle image density must be high enough to provide a sufficient number of image pairs for successful interrogation in all spots throughout the region of interest. The last of these requirements is typically the most difficult to satisfy and generally governs the choice of spot size, and thus, spatial resolution.

Results

Interrogation System Validation

Validation of the PIV system first involved testing of the interrogation system. As a first check on the accuracy of the autocorrelation output and the associated image processing software, an interrogation was performed on a known uniform dot pattern with a spacing of 133 dots/in. in both the horizontal and vertical directions. The pattern is a commercially produced screen PMT for making copies of photographic prints. The screen was used in place of a PIV photograph on the interrogation system and was interrogated several times at various magnifications, storing both the dot pattern image input and the autocorrelation output. After analysis, peaks in the spatial autocorrelation output were compared to the original dot pattern. The spacing of peaks in the autocorrelation output was found to match the center spacing of the original dot pattern to within 1%. This is expected for a uniform pattern since each dot correlates perfectly with itself, the closest neighbor in each direction, the second closest neighbor, etc.

Table 1 Uniform displacement photograph interrogation results

	Photo 1	Photo 2
$\overline{\Delta x}$,[a] μm	63.515	131.299
$\overline{\Delta y}$,[b] μm	58.523	133.153
$\sigma_{\Delta x}$, μm	2.001	1.166
$\sigma_{\Delta y}$, μm	1.929	2.153
$\sigma_{\Delta x}/d_p$, %	5.72	6.19
$\sigma_{\Delta y}/d_p$, %	5.51	6.15
$\overline{\lvert \Delta X \rvert}$,[c] μm	86.366	187.000
$\overline{\lvert \Delta X \rvert}_{\text{actual}}$, μm	87	187
Interrogation spot, mm		0.8×0.8
Increment, mm		0.4
Total spots/photo		10,000
Image pairs/spot		~8
Mean image diameter, d_p, μm		~35

[a]Mean interrogated x displacement.
[b]Mean interrogated y displacement.
[c]$\overline{\lvert \Delta X \rvert} = [(\overline{\Delta x})^2 + (\overline{\Delta y})^2]^{1/2}$.

Tests were then done with known displacement simulated PIV photographs. The most accurate simulation used photographs of uniformly displaced image pairs. The photographs were made by first printing a randomly spaced dot pattern on an $8\frac{1}{2} \times 11$ in. sheet. A photograph of the unpaired images was then made on 4×5 in. Kodak Technical Pan 4415 film in an enlarger. This unpaired-dot photograph (clear dots on a dark background) was then attached to a translation stage and placed over unexposed film for contact printing. Exposures were made with the unpaired-dot photograph in an initial position and in a second position, displaced by the translation stage, insuring uniform image pair displacements. The resulting paired-dot photograph (dark dot pairs on a clear background) was then contact printed onto film, resulting in the final paired-dot photograph (clear dot pairs on a dark background). Two photographs were made with different displacements. The photographs were examined under a 14X stereo microscope equipped with a measuring reticule marked in 5 μm increments to determine the actual mean displacements of 87 and 187 μm as presented in Table 1. Both photographs started with a pseudo-randomly dispersed pattern of approximately 12.5 image pairs/mm^2, but due to nonuniformity in the pseudo-random dot dispersion, film flatness, film sensitivity, lighting, dust, etc., the image density on the final photographs was reduced and varied throughout the photographs. Image diameters also varied from 20 to 50 μm due to the same photographic effects. This variation in image density, image size, and other effects due to the printing of the images on film creates a good simulation of real PIV photographs, except for the lack of unpaired images which occur in real flowfield photographs due to some particles moving out of the laser sheet between pulses.

Interrogations were made of each photograph at 10,000 locations with the results presented in Table 1. The statistics shown were calculated using only "good" data falling within ± 17 μm of the mean displacement in each direction, which was over 90% of the total for both photographs. The deviation from 100% good data was due to the aforementioned dot dispersion and photographic effects which reduced image density in some areas. Bad vector replacement and smoothing were not done in order to preserve the full error in the interrogation. The photographs were interrogated with the direction of displacement at approximately a 45-deg angle to the horizontal to examine the dependence of error on variations in both the x- and y-displacement magnitudes. The data reveal that the standard deviation of the interrogated displacements is approximately constant at 2 μm for both photographs. This is an expected result since the random error in displacement should be proportional to the particle image diameter and not the magnitude of displacement.[7] Given the mean image diameter d_p of 35 μm, the random error is approximately 6% of d_p. It should be noted that although photographic imperfections and other factors in real PIV photographs may tend to increase this error ratio, the use of vector field smoothing tends to reduce the random error significantly as mentioned in the preceding discussion of the interrogation system. The mean interrogated displacement for photograph 2 is taken as exactly 187 μm since it was used as the reference for determining the pixel-to-μm scaling factor. The mean interrogated displacement for photograph 1 matches the actual displacement to within 1%, which is within the error in the measurement of the actual displacements, showing no evidence of mean bias error.

Low-Speed Round Jet

The full PIV system has been used to examine the flow from a round free jet test stand consisting of a 6 in. long, 1 in. o.d. tube fed by a TSI six-jet atomizer with silicone oil seed and an adjustable dilution air supply as shown in Fig. 5. The jet flows into an $8 \times 10 \times 48$ in. test section exhausted to atmosphere. Image shifted PIV photographs were taken on both 35 mm and 4×5 in. film. Although the jet velocity was relatively low, experiments done with this test stand used the same equipment

and procedures that are used for high-speed flow experiments, including seeding, laser system, birefringent image shifting optics, Kodak Technical Pan film, automated system operation, and high spatial resolution of velocity measurements. The sole differences involve the seeder supply pressure and film formats for the data presented. Reduced seeder pressure (5–10 psig vs 20 psig for high-speed flow experiments) was necessary to avoid damage to the low-speed test section, but the effect of lower pressure and flow rate tends to reduce the mean seed particle size. This is because atomized droplets must rise against gravity to leave the atomizing chamber, and the reduced flowrate carries fewer heavy particles out. The data presented for these experiments was also taken on 4 × 5 in. film while subsequent high-speed flow experiments used 35-mm film for convenience, since film grain and image size limitations were found to be acceptable. The main purpose of these low-speed flow experiments was to demonstrate the operation and data analysis capabilities of the system.

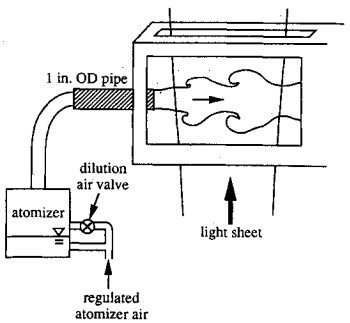

Fig. 5 Round jet test stand used for initial low-speed flow application of PIV system.

Particle image sizes were measured from the photographs for determination of the minimum measurable particle displacement, which must be at least one image diameter to prevent overlap of pairs. Average image diameters were approximately 55 μm for 35-mm photographs and 35 μm for 4 × 5 in. photographs (in the frame of reference of the flowfield). For a projected interrogation spot size of approximately 1 mm^2, for which the maximum measurable displacement is approximately 250 μm (see preceding discussion of spatial resolution), this provides quite sufficient dynamic range, where the dynamic range is the ratio of the maximum to the minimum measurable displacement.

Determination of the mean image diameter also provides the ability to estimate the random error of velocity measurements. Using the information from the validation experiment reported in Table 1, the standard deviation of the random error is expected to be 6% of the mean image diameter, or 3.3 μm for the 35-mm photographs and 2.1 μm for the 4 × 5 in. photographs. With a maximum image displacement of approximately 250 μm (selected by choosing the time delay between laser pulses), the random error is 1.3% or 0.8% of the maxi-

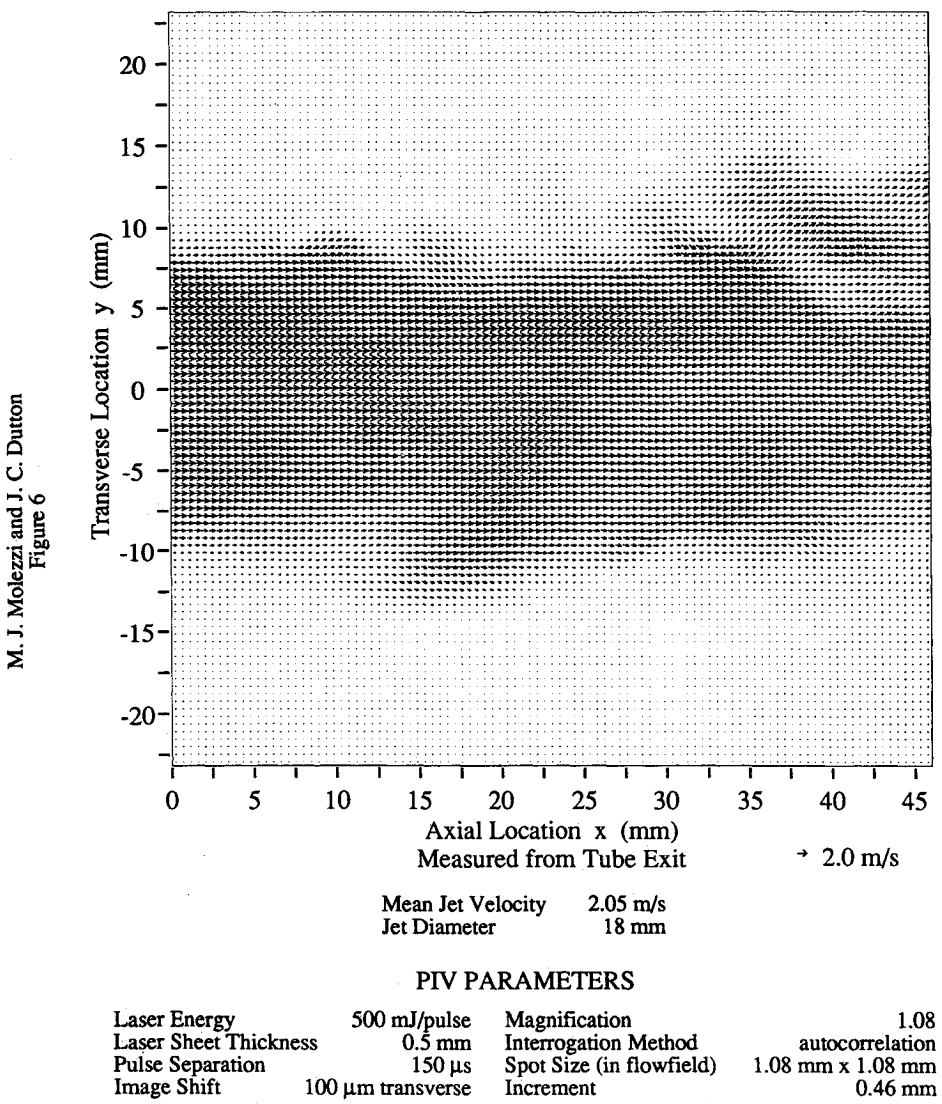

Fig. 6 Round jet velocity field: initial application of PIV system in low-speed jet flow.

mum velocity (proportional to image displacement) for 35-mm photographs or 4×5 in. photographs, respectively.

An example PIV photograph of the jet was then interrogated. This photograph was taken using Kodak Technical Pan 4415 4×5 in. film with a 120-mm lens at f 5.6. Other parameters for acquisition and interrogation are shown in Fig. 6. Before a full interrogation was done, the repeatability of the measurements was checked by interrogating a small region of the photograph, then resetting the positioner to its original position and reinterrogating. The results showed perfect agreement of both the first and second peak locations for the entire 4×4 grid of interrogation spots. Only the first two autocorrelation peaks were stored for this interrogation which was done before third peak storage was implemented. Reinterrogation was also done on two 5×5 regions (total of 50 spots) after the full interrogation was completed, involving a positioner travel of more than 25 mm in each direction. This resulted in 28 matches of both the first and second highest autocorrelation peaks, 18 matches of the first peak only, and 4 nonmatches. It should be noted that exact peak locations can vary due to bidirectional positioner error over long travel distances (±10 μm over 7-mm travel) and random electronic noise in video imaging.

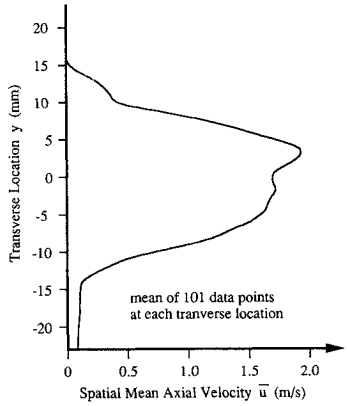

Fig. 7 Round jet spatial mean velocity: mean velocity at each transverse location of Fig. 6.

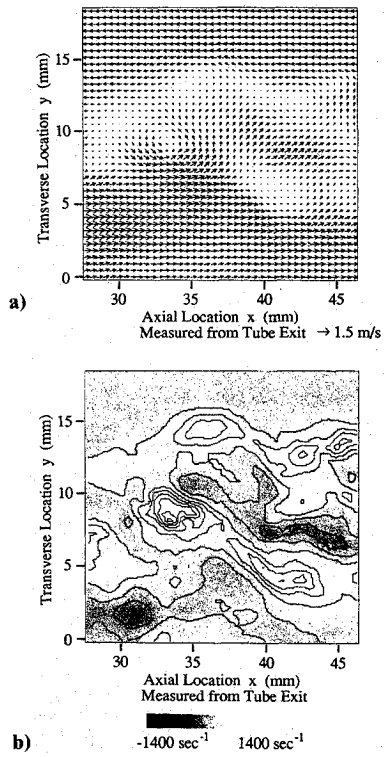

Fig. 8 Enlarged section of round jet: a) velocity field with 0.68-m/s axial velocity subtracted to accent flow structure; b) vorticity field derived from velocity data (grayscale and overlaid contours).

Fig. 9 Schlieren photograph of flow past a finite thickness base, $M_\infty = 0.4$ (from Ref. 13).

Removal and interpolation of bad vectors for the full flowfield showed a success rate for valid vector determination of approximately 94%, which is quite reasonable in comparison to other reported success rates. The final velocity vector plot after subtraction of image shift, interpolation, and smoothing is shown in Fig. 6. The photograph was interrogated over a 46×46 mm area with 0.46-mm increments in each direction, resulting in 10,201 vectors (101×101). The interrogation increment is chosen to be approximately half the spot dimension to avoid aliasing of high spatial frequency velocity fluctuations. The full interrogation took 11 h, 18 min or 4.0 s/spot using the autocorrelation method. Interrogations using the Young's fringe method took 2.3 s/spot.

The mean velocity at the tube exit is approximately 2.05 m/s. Examination of Fig. 6 shows typical vortex structures at the edges of the jet with a gradual decrease in the centerline velocity as the jet propagates downstream. A plot of the spatially averaged axial velocity component at each transverse location is shown in Fig. 7. Although this spatial mean is not equivalent to a time average velocity profile due to spreading of the jet over the field of view, it does reveal a general nonuniformity of the flow, implying that the jet is not truly axisymmetric. The higher velocity at the top of the tube was induced by the flow around a bend in the flexible tubing just before the straight section at the jet exit. Although the test flow is not ideal, the ability to reveal such information is part of the purpose of this experiment.

Identification of flow structures can also be done by manipulating the acquired velocity data. The vortex structure in the upper right section of Fig. 6 is shown in Fig. 8a with a portion of the mean axial velocity subtracted and in Fig. 8b by deriving the out-of-plane vorticity $\{\partial v/\partial x - \partial u/\partial y\}$ from central finite differences of the original velocity data. Both reveal the expected dominant positive (counterclockwise) vorticity at the upper edge of the jet and some resulting negative (clockwise) vorticity between structures. The ability to obtain spatially well-resolved velocity data for such analysis allows quantification of turbulent flow structures by determination of vortex strength and position. Similar analysis can be performed with rate-of-strain, volumetric flux, and other derivative and integral quantities important in a particular flowfield to provide information about the nature of complex high-speed flows.

Low-pass and high-pass spatial filtering can also be done[10] to reveal both large- and small-scale structures.

High-Speed Base Flow

Two-dimensional finite thickness bodies in subsonic and transonic flows form a separated flowfield very rich in turbulent structure due to the presence of the well-known von Kármán vortex street wake. The schlieren photograph in Fig. 9 shows the wake behind a blunt base in a Mach 0.4 freestream. The screw visible in the photograph was used for focusing and is outside of the test section. The motivation for studying this flow with PIV stems from both the fact that it exhibits a well-defined instantaneous structure and that the mechanism of the observed base drag reduction in the presence of a base cavity is not completely understood.[11-15] To resolve discrepancies in previous work on this subject and to better define the mechanisms of base cavity drag reduction, PIV experiments are being done to quantify flow structure for various freestream Mach numbers and base configurations.

Modifications have been made to an existing transonic wind tunnel for the use of PIV on two-dimensional base flows (Fig. 10). The previously fabricated tunnel has a 4×4 in. test section with solid side walls and slotted upper and lower inner walls to relieve the blockage effect of models in the transonic speed range. To allow visualization past the aft end of base models 6-in.-diam round windows are mounted in both sidewalls. The base model consists of interchangeable afterbodies mounted on a 15.24-mm-thick wedge-shaped forebody, with its upstream edge located approximately 17 in. downstream of the nozzle entrance. The afterbodies include a solid base, a rectangular cavity base with a depth of half the base height, and a rectangular cavity base with a depth of one full base height.

Slot-shaped upper and lower windows have been fabricated and installed in the outer tunnel walls for access with a vertically propagating planar laser sheet for PIV. The sheet passes through the lower window and through one of the streamwise slots of the inner wall to enter the test section. The seed delivery is done by two TSI six-jet atomizers feeding a single ¾-in. o.d. tube that enters the stagnation chamber. This tube leads to a manifold tube that feeds eight smaller tubes directed downstream and oriented in a transverse (vertical) plane aligned with the illuminating laser sheet. The flow then passes through 2-in. long, 3/16-in. cell honeycomb and a 44×44 mesh screen with 57% open area to reduce turbulent fluctuations in the supply flow. It should be noted that the screen is cut out in the areas where the seed tubes feed through the honeycomb. This is done because experience with LDV in this laboratory has shown that silicone oil droplets tend to build up on any surface perpendicular to the flow direction, causing large drops to form and burst off, which bias velocity measurements. Flow seeding behind the base is sufficient due to small seed particle slip velocity allowing the motion of the alternating von Kármán vortex street to carry seed into the wake.

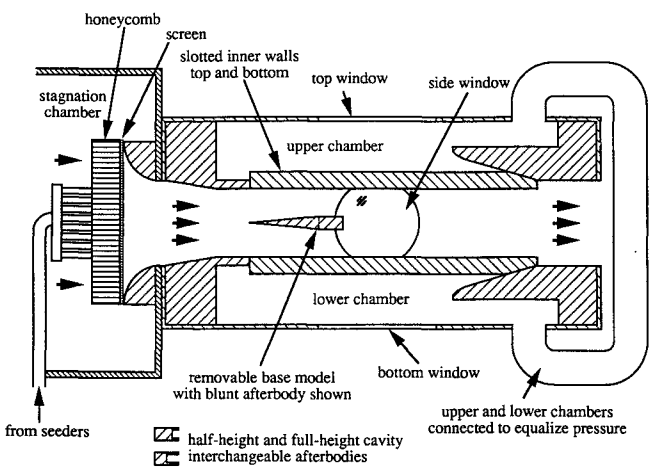

Fig. 10 Transonic wind tunnel with slotted-wall test section and two-dimensional base model.

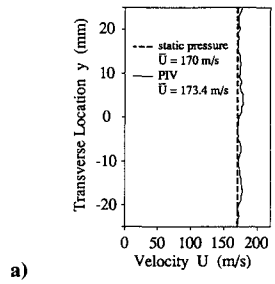

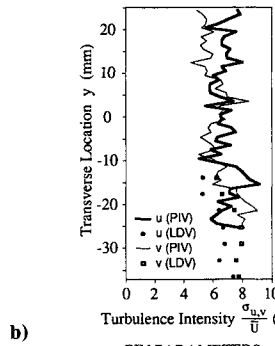

PIV PARAMETERS

Laser Energy	450 mJ/pulse
Laser Sheet Thickness	0.5 mm
Pulse Separation	1.1 μs
Image Shift	none
Magnification	0.3
Interrogation Method	autocorrelation
Spot Size (in flowfield)	1.3 mm x 1.3 mm
Increment	1 mm

Fig. 11 PIV data validation results from uniform Mach 0.5 flow: a) PIV spatial mean velocity vs temporal mean velocity from pressure data; b) turbulence intensity: PIV spatial data vs LDV temporal data.

The first experiments in this facility were done without a base model to compare PIV velocity measurements to data obtained with both LDV and static pressure taps. PIV photographs were taken on 35-mm Kodak Technical Pan 2415 film. To facilitate comparison to the time-integrated pressure and LDV measurements of velocity, PIV velocity data from a single photograph were summed along the row at each transverse location to obtain mean velocity components and standard deviations were found to determine turbulence intensities. Given that the flowfield is not evolving in the streamwise direction in this tunnel-empty case, equating spatial statistics to temporal statistics is adequate for a first approximation, although the number of samples available from a single PIV photograph is not sufficient for highly accurate statistics. It should be noted that there were not yet any flow conditioning devices in the wind tunnel when these experiments were done, the effects of which will be discussed in the following paragraphs.

The results for mean velocity from a run at Mach 0.5 are shown in Fig. 11a with the relevant PIV parameters. The PIV data are compared to the mean velocity calculated with pressure data from taps measuring static pressure in the test section and total pressure in the stagnation chamber. Although there are at most only 81 PIV measurements per data point in this plot, the mean velocity at each transverse location varies only slightly from the overall mean of 173.4 m/s, which is within 2% of the mean velocity determined from the pressure measurements.

A more stringent test of the accuracy of PIV lies in the ability to measure velocity fluctuations. To this end, LDV measurements of streamwise and transverse turbulence intensity were made for comparison to the PIV data (Fig. 11b). Because of the spatial constraint of avoiding contact between the LDV laser and the lower wall of the wind tunnel, LDV measurements could only be made up to a transverse location of -12.5 mm measured from the test section centerline.

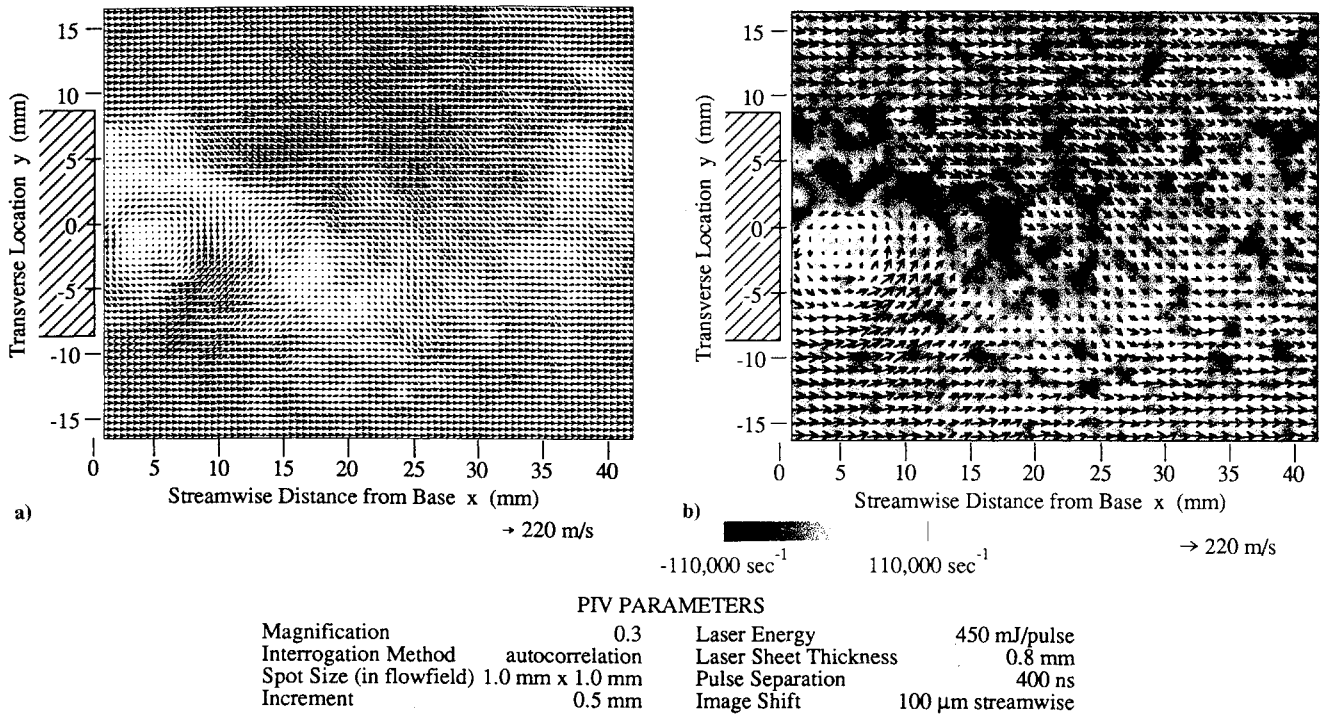

Fig. 12 Two-dimensional base flow PIV results at $M_\infty = 0.4$: a) velocity field with full resolution; b) vorticity (grayscale) with velocity field overlay (reduced resolution for clarity).

Again, a maximum of only 81 PIV measurements was used for the data at each transverse location, but it can be seen from the plot that both the LDV and PIV data vary from 5 to 8% turbulence intensity. Although this data lends some confidence in the accuracy of the PIV data, it revealed undesirable freestream turbulence in the test section without flow conditioning. The aforementioned honeycomb and screen were therefore added to the facility. PIV measurements of turbulence intensity with the flow conditioning devices installed have shown turbulence intensities of 3–5% which, while improved, are still relatively high. Although LDV measurements with flow conditioning have not yet been made due to restrictions on the availability of the LDV system, the high turbulence intensity measured by PIV is quite likely due to turbulence generated downstream of the honeycomb and screen by the velocity gradients between the freestream and the lower velocity seeded jets.

Experiments have most recently been done with a solid base model in a Mach 0.4 freestream. The Mach 0.4 freestream condition is determined by running the test section at a stagnation pressure that results in a Mach 0.4 flow when no model is present. PIV photographs using birefringent image shifting were taken on 35-mm Kodak Technical Pan 2415 film. The mean image diameter for the photos is approximately 40–50 μm in the frame of reference of the flowfield. Using the error data from the validation results presented in Table 1, the random measurement error is expected to be approximately 6% of the mean image diameter, or less than 1.6% of the maximum particle image displacement.

The interpolated and smoothed velocity plot for a region spanning approximately 2.7 base heights downstream of the base edge is shown in Fig. 12a. The location of the base is indicated by the cross-hatched region. The plot includes 5346 vectors (81 × 66) with an increment of 0.5 mm between vectors and a square interrogation spot of 1.0 mm^2. As with the round jet data, the increment is chosen to be approximately half the interrogation spot dimension to avoid aliasing of high spatial frequency velocity fluctuations. The total interrogation time was 6 h, 15 min or 4.2 s/spot using the autocorrelation method. The success rate for valid vector determination was 80% overall including edge regions where seed density dropped off, and approximately 90% in the wake region within the upper and lower edges of the base. The presence of interrogated particle images at the vortex centers also indicates that submicron oil droplets are being recorded on film since centripetal acceleration forces all but the smallest particles out of the vortex centers as they travel downstream. Using an estimate from Fig. 12 of the centripetal acceleration in a vortex and using the Stokes flow drag law, the slip velocity of a 1 μm diam silicone oil sphere was found to be approximately 15 m/s, which would carry the particle more than 2 mm away from the vortex center by the time it moves one base height downstream of the base edge. Therefore, the velocity data obtained at the vortex centers must be obtained from submicron particles.

Figure 12a includes all interrogated velocity vectors to indicate the full resolution of the measurements. Although the wake structure is somewhat evident in Fig. 12a, it is accentuated in Fig. 12b which has the velocity vector field overlaid on a grayscale representation of the vorticity. Only every other vector is plotted in Fig. 12b in the interest of clarity. The vorticity plot reveals the fragmentation of the main vortices and the presence of lower intensity small-scale turbulent structures of about 3 mm diameter throughout the flowfield. The source of these structures is presently unknown. They may be due to high freestream turbulence levels, but an estimate of the Taylor microscale for this flowfield using mean velocity gradient data was found to be 2.67 mm, suggesting that the structures may be a secondary feature of the vortex street wake. Additional data is required with reduced freestream turbulence levels and various freestream velocities to make a more definite determination, but the more important fact at this point is that the PIV technique has shown the capability to reveal and quantify flowfield structure not found in previous work.

Conclusion

A complete PIV system has been developed for application in separated high-speed flows. Successful demonstration in both low- and high-speed flow validation experiments along with analysis of known displacement photographs has shown the capability for accurate velocity measurement with the use

of submicron seed particles and birefringent image shifting. Analysis of a high-speed separated flowfield has also been done with a spatial resolution of 1.0 mm^2 per interrogation spot (measured in the flowfield frame of reference). This improvement in the spatial resolution of the PIV technique in compressible flows increases the capability for determination and quantification of small-scale turbulent structures and stands to provide important data for turbulence modeling, numerical simulations, and analysis of complex flowfields.

Future work in the area of subsonic and transonic base flows will concentrate on reduction of freestream turbulence, adjustment of the acquisition system optics for improved performance, and improvement of seeding uniformity, which has been the most challenging problem to this point. The result will be a quantitative analysis of base cavity effects on wake structure for the determination of the fluid dynamic mechanisms governing base cavity drag reduction.

Acknowledgments

The authors gratefully acknowledge the support of the U.S. Army Research Office through Thomas L. Doligalski and the University of Illinois in funding this research. The authors also wish to extend thanks to Ronald A. Rosner for his work in developing the interrogation software and to R. J. Adrian, R. D. Keane, P. W. Offutt, and A. K. Prasad of the Department of Theoretical and Applied Mechanics, University of Illinois at Urbana-Champaign, for their useful advice in the development of this system.

References

[1]Miles, R. B., Connors, J. J., Markovitz, E. C., Howard, P. J., and Roth, G. J., "Instantaneous Profiles and Turbulence Statistics of Supersonic Free Shear Layers by Raman Excitation Plus Laser-Induced Electronic Fluorescence (RELIEF) Velocity Tagging of Oxygen," *Experiments in Fluids,* Vol. 8, No. 1-2, 1989, pp. 17-24.

[2]Palmer, J., McMillin, B., and Hanson, R., "Planar Laser-Induced Fluorescence Imaging of Velocity and Temperature in Shock Tunnel Free Jet Flow," AIAA 30th Aerospace Sciences Meeting, AIAA Paper 92-0762, Reno, NV, Jan. 1992.

[3]Kompenhans, J., and Höcker, R., "Application of Particle Image Velocimetry to High Speed Flows," *Von Kármán Institute Lecture Series 1988-06,* Von Kármán Inst., Brussels, Belgium, March 1988, pp. 67-83.

[4]Höcker, R., and Kompenhans, J., "Application of Particle Image Velocimetry to Transonic Flows," *Proceedings, Fifth International Symposium on Applications of Laser Techniques to Fluid Mechanics,* Springer-Verlag, Berlin, 1990, pp. 415-434.

[5]Post, M. E., Goss, L. P., and Brainard, L. F., "Two-Color Particle-Imaging Velocimetry in a Turbine Cascade," AIAA 29th Aerospace Sciences Meeting, AIAA Paper 91-0274, Reno, NV, Jan. 1991.

[6]Landreth, C. C., and Adrian, R. J., "Electrooptical Image Shifting for Particle Image Velocimetry," *Applied Optics,* Vol. 27, No. 20, 1988, pp. 4216-4220.

[7]Adrian, R. J., "Particle-Imaging Techniques for Experimental Fluid Mechanics," *Annual Review of Fluid Mechanics,* Vol. 23, 1991, pp. 261-304.

[8]Landreth, C. C., and Adrian, R. J., "Measurement and Refinement of Velocity Data Using High Image Density Analysis in Particle Image Velocimetry," *Proceedings, Fourth International Symposium on Applications of Laser Anemometry to Fluid Mechanics,* Springer-Verlag, Berlin, July 1988, pp. 485-497.

[9]Bloomberg, J. E., "An Investigation of Particle Dynamics Effects Related to LDV Measurements in Compressible Flows," M.S. Thesis, Dept. of Mechanical and Industrial Engineering, Univ. of Illinois at Urbana-Champaign, Urbana, IL, May 1989.

[10]Reuss, D. L., Adrian, R. J., Landreth, C. C., French, D. T., and Fansler, T. D., "Instantaneous Planar Measurements of Velocity and Large-Scale Vorticity and Strain Rate in an Engine Using Particle-Image Velocimetry," SAE International Congress and Exposition, Paper 890616, Detroit, MI, Feb. 27-March 3, 1989.

[11]Pollock, N., "Some Effects of Base Geometry on Two-Dimensional Base Drag at Subsonic and Transonic Speeds," Australian Aeronautical Research Lab., Aerodynamics Note 316, Melbourne, Australia, Oct. 1969.

[12]Nash, J. F., Quincey, V. G., and Callinan, J., "Experiments on Two-Dimensional Base Flow at Subsonic and Transonic Speeds," Aeronautical Research Council, R&M 3427, England, UK, Jan. 1963.

[13]Kruiswyk, R. W., and Dutton, J. C., "Effects of a Base Cavity on Subsonic Near-Wake Flow," *AIAA Journal,* Vol. 28, No. 11, 1990, pp. 1885-1893.

[14]Rudy, D. H., "A Numerical Study of Unsteady Two-Dimensional Subsonic Compressible Base Flow," Ph.D. Dissertation, Dept. of Mechanical and Industrial Engineering, Univ. of Illinois at Urbana-Champaign, Urbana, IL, April 1987.

[15]Clements, R. R., and Maull, D. J., "The Representation of Sheets of Vorticity by Discrete Vortices," *Progress in Aerospace Science,* Vol. 16, No. 2, 1975, pp. 129-146.